AAS 24-013

RETINA: A HIGHLY-VERSATILE OPTICAL FACILITY FOR CAMERA-IN-THE-LOOP TESTING OF SPACEBORNE VISION-BASED SENSORS

Fabio Ornati[*], Paolo Panicucci[†], Eleonora Andreis[‡] and Francesco Topputo[§]

The increasing number of deep-space missions and the consequent saturation of the Deep-Space Network navigation slots has sparked the interest in autonomous navigation techniques. Among these, vision-based algorithms seem the most promising for providing accurate navigation solutions using low-cost, lightweight, and reliable sensors. In order to verify the performance and robustness of the navigation software and hardware, the conditions of the space environment shall be emulated and simulated on the ground. This paper presents the design of a new hardware-in-the-loop facility for performing testing and validation of optical navigation sensors. The facility architecture features variable magnification, allowing the deployment of cameras with a wide range of field-of-view, while retaining the high-quality imaging typical of fixed magnification test benches. The paper discusses the design drivers and proposes a cost-effective setup that uses only commercial-off-the-shelf components. New calibration strategies for achieving a more accurate reproduction of the space scenes are detailed. The performance of the facility is analyzed in terms of image quality, geometrical accuracy, and radiometric fidelity.

INTRODUCTION

Validation and verification of Vision-Based Sensors (VBSs) for space-borne applications is a burdensome activity, both in economic and technological terms. New hardware and software require detailed testing since the early phases of their development to increment their Technology Readiness Levels (TRLs), validate functionalities, and characterize bugs or unexpected behaviors. These tests are usually conducted inside Hardware-In-the-Loop (HIL) facilities which allow the synthetic reproduction of the visual conditions that would be met while in orbit.

A discrete number of such testbeds have been developed in the past years and discussed in literature.[1–8] All of them are characterized by the presence of two fundamental components: a screen for stimulating the VBS with synthetic scenes and a corrective optical equipment. In particular, one or more refractive lenses are placed between the deployed VBS and the screen to collimate its light. In

[*]PhD Student, Department of Aerospace Science and Technology, Politecnico di Milano, Via La Masa 34, 20156, Milan, Italy, fabio.ornati@polimi.it.

[†]Assistant Professor, Department of Aerospace Science and Technology, Politecnico di Milano, Via La Masa 34, 20156, Milan, Italy, paolo.panicucci@polimi.it.

[‡]PhD Student, Department of Aerospace Science and Technology, Politecnico di Milano, Via La Masa 34, 20156, Milan, Italy, eleonora.andreis@polimi.it.

[§]Full Professor, Department of Aerospace Science and Technology, Politecnico di Milano, Via La Masa 34, 20156, Milan, Italy, francesco.topputo@polimi.it.

this way, the scene observed by the VBS is projected to infinity, reproducing the characteristics of light coming from far-range objects.[1]

Depending on the purpose of the tests, the reproduced scenes may involve static and dynamic simulations of night skies, celestial bodies, and satellites at various ranges. Such diversity of applications often implies the use of VBSs with different imaging characteristics (e.g., focal length, sensor size, resolution). The simplest testbeds are fixed magnification facilities where a single lens collimates the light coming from the screen to stimulate the camera. In fixed magnification facilities, the focal length of the collimating optics must be accurately selected in order to meet the requirements dictated by the testing hardware.[1,7] Because of this, fixed magnification test beds are specifically designed for a particular VBS and do not allow for the use of cameras with different Field-of-View (FoV). If a different VBS needs to be used a different collimator must be selected and purchased, implying delays and costs. This lack of versatility is overcome by using variable-magnification facilities. These include variable-magnification lens systems that guarantee the optimal matching between the screen size and the camera FoV in any working condition.[7]

RETINA (Realistic Experimental faciliTy for vIsion-based NAvigation) is a novel variable magnification Hardware-In-the-Loop testbed assembled by the Deep-space Astrodynamics Research and Technology (DART)* group at Politecnico di Milano. The facility will support the development and validation of the autonomous Vision-Based Navigation (VBN) and Image Processing (IP) pipeline within the first pillar of the ERC-funded EXTREMA (Engineering Extremely Rare Events in Astrodynamics for Deep-Space Missions in Autonomy) project.[9–13] In the future, the testbed will host the HIL simulations of the LUMIO Cam, the main payload of the LUMIO mission, deemed at the detection of meteoroid flashes from the lunar far side.[14–16]

This paper is structured as follows. Section "Facility design" discusses the requirements and the constraints impacting the design of the facility. An optimized lens design is proposed and analyzed. Section "Calibration" presents the radiometric and geometric calibration procedures used to ensure realistic reproduction of the visual conditions and the performance reached in terms of accuracy. Section "Applications" shows examples of vision-based navigation and attitude reconstruction simulations conducted with the facility. In the last section, conclusions are drawn.

FACILITY DESIGN

Architecture and components

The RETINA facility has been designed with the intent of creating a versatile test bench for stimulating CubeSats-compatible vision-based navigation sensors. These are in general characterized by small detector sizes to reduce the overall size and weight and by a wide range of FoV values. The variable magnification characteristic of RETINA allows the deployment of cameras with different FoVs without the need to modify the hardware of the facility. In particular, the operational diagonal FoV range of the facility has been chosen between 4 and 22 degrees. This range is compatible with the simulation of both the LUMIO Cam[14] and the lower-end portion of the star-tracker camera FoVs.

RETINA is composed of several opto-mechanical parts installed onto a 60 x 120 cm optical bench. The entire facility is enclosed in a dark room to prevent disturbances and reflections from external light sources. The architecture has been derived from the one developed by Beierle et al[7]

*DART group web-page: `https://dart.polimi.it/`, last visited on Jan 2024

Table 1. Characteristics of VBS configurations

Configuration	Focal length (mm)	FoV (deg)	Diagonal FoV (deg)
Wide-FoV	25	12.1 x 16.1	20.0
Narrow-FoV	25	6.07 x 8.08	10.1

and includes the following components:

1. A WUXGA R5* OLED display.
2. A collimator lens system to project the observed scenes at infinity.
3. A relay lens assembly to achieve variable magnification capabilities.
4. A camera and objective that mimic the characteristics of real VBSs.

The screen has been specifically selected for its small size (18.7 x 11.75 mm) and high resolution (1920 x 1200 pixels). Since it relies upon OLED (Organic Light Emitting Diode) technology, it can achieve an extremely high dynamic range with virtually inexistent backlight leakage. These features are especially beneficial considering that the purpose of the facility is to simulate optical navigation scenarios that involve celestial objects with large differences in magnitude levels. The VBS used throughout the tests of this paper is a FLIR BFS-U3-31S4† monochrome camera with a 1536 x 2046 pixel 1/1.8" sensor. Two objective configurations named wide-FoV and narrow-FoV are used. Their characteristics are reported in Table 1.

The two lens groups are mounted onto movable optical stages that can be manually adjusted in three axes with micrometric precision. The optical behavior of the facility can be understood by looking in detail at each component in the simplified paraxial lens scheme of Figure 1. The collimator, which has a focal length f_c, is placed exactly one focal length away from the location of the virtual image of the screen generated by the relay lens. In this way, the scene observed by the VBS is projected at infinity, as in the case of distant objects in space.[1,7] The size of the relayed image (h_i) depends on the magnification level M. If h_s is the size of the screen, then:

$$h_i = -Mh_s \tag{1}$$

The optimal working condition occurs when the camera observes the screen in its entirety. In this case, the resolution of the scenes is maximized and every portion of the camera FoV can be stimulated by a pixel on the screen. To achieve this condition, the size of the relayed image h_i must match the size of the camera FoV. Using trigonometry, it is easy to obtain that:

$$h_i = 2f_c \tan\left(\frac{\text{FoV}}{2}\right) \tag{2}$$

Thanks to equations (1) and (2), one can determine the magnification needed to achieve the matching condition:

*WUXGA-R5 spec-sheet: `www.emagin.com/products/WUXGA`, last visited on Jan 2024.

†FLIR BFS-U3-31S4 spec-sheet: `http://softwareservices.flir.com/BFS-U3-31S4/latest/Model/spec.html`, last visited on Jan 2024.

$$M = -2\frac{f_c}{h_s}\tan\left(\frac{\mathrm{FoV}}{2}\right) \tag{3}$$

Paraxial constraint analisys

The magnification M determines the distances between the screen and the relay lens s_{or} and between the relay lens and the virtual image s_{ri}:[7]

$$s_{or} = \left(\frac{M-1}{M}\right) f_r \tag{4}$$

$$s_{ri} = (1-M) f_r \tag{5}$$

Therefore, the total length occupied by the optical system in the facility is:

$$s_{oc} = s_{or} + s_{rc} = s_{or} + s_{ri} + f_c \tag{6}$$

The size of the optical bench poses a constraint regarding the maximum allowed total length. In particular, this is limited to $s_{oc}^{max} = 850$ mm to guarantee compatibility with the enclosure and the other components. Two additional constraints are determined by the mechanical setup of the facility. These are: the minimum screen-relay lens distance ($s_{or}^{min} = 100$ mm) and the minimum inter-lens distance ($s_{rc}^{min} = 100$ mm).

One of the main optical requirements for the facility is to have the entrance pupil of the deployed VBS overfilled in any possible working condition. This avoids the appearance of vignetting in the simulated images. When vignetting occurs, part of the light that should reach the sensor is blocked as it travels outside one of two lenses. Since this effect is angle-dependent, it would lead to the acquisition of pictures affected by a significant and unrealistic loss of illumination at their edges.

Consider the light paths as sketched in Figure 1. R_r and R_c are the radii of the relay and collimator lenses, respectively, and d_{cam} is the diameter of the VBS entrance pupil. The two orange rays

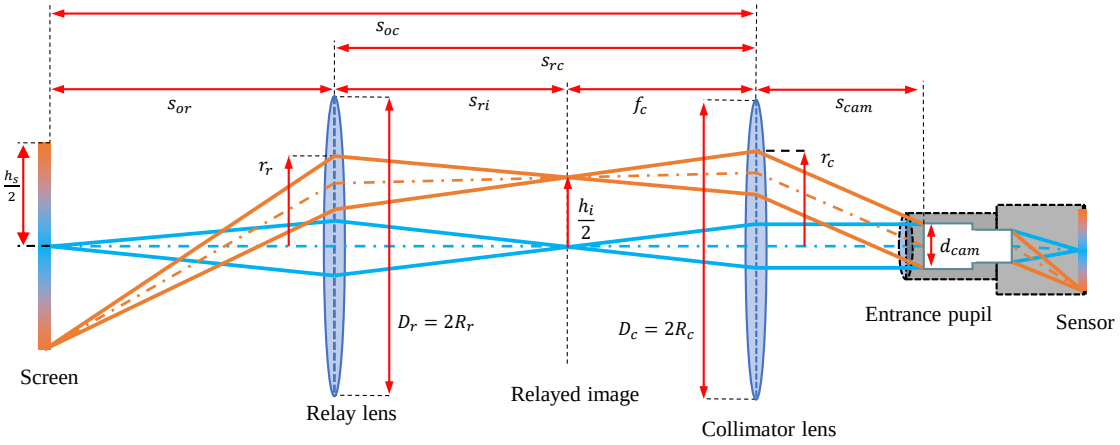

Figure 1. Paraxial model of the optical system.

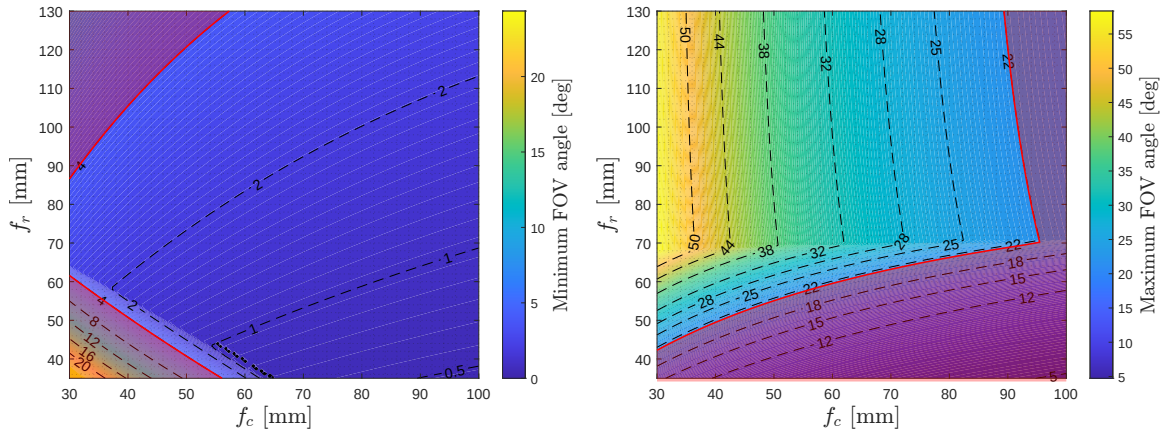

(a) Minimum FoV (b) Maximum FoV

Figure 2. Minimum (a) and maximum (b) allowable FoV angles that satisfy all the constraints. Red areas do not satisfy design requirements.

identify the boundaries of the light ray field associated with the maximum FoV of the VBS. It is easy to verify that no vignetting occurs as long as the path of those rays does not exit the diameter of the two lenses. In other words, that is when $r_r < R_r$ and $r_c < R_c$, where r_r and r_c are the further distances from the optical axis at which the two rays cross the relay and collimator lenses, respectively.

The values of r_r and r_c can be computed through paraxial geometric ray-tracing for a given combination of FoV angle, pupil aperture d_{cam}, lenses focal lengths, and intra-lens distances. Incidentally, all the distances but s_{cam} have a dependence upon the FoV of the VBS and the focal lengths, as shown in Equations (4)-(6). Therefore, by considering the two lenses' focal lengths as the only design variables, it is possible to find the range of FoV angles for which the mechanical and vignetting constraints are satisfied. The FoV range is numerically computed for a set of f_c-f_r focal length combinations. The results of this analysis are presented in Figure 2, which shows the minimum and maximum allowable FoV angles for each combination. The results are computed considering a pupil aperture of $d_{\text{cam}} = 10$ mm and a lens diameter of $D_r = D_c = 2$". Note that these settings only affect the vignetting constraint which limits the maximum FoV angle. The distance between the VBS pupil and the collimator lens s_{cam} is set equal to the collimator focal length f_c. This value is approximately the one that minimizes the chances of vignetting for two lenses having the same diameter.

The zones of the Figures and highlighted in red identify the combinations of focal lengths in correspondence with which the maximum and minimum FoV requirements cannot be satisfied without violating either the mechanical or the vignetting constraints. These results are used to initialize the optical design of the facility and determine the set of suitable focal length combinations.

Optical design

A simple paraxial lens model does not give any information about optical aberrations and therefore cannot predict the optical performance of the facility. For this reason, a commercial optical design software (i.e., Zemax OpticStudio*) is used for determining the best design for the facil-

*Zemax OpticStudio® web-page: `www.zemax.com/opticstudio`, last visited on Jan 2024.

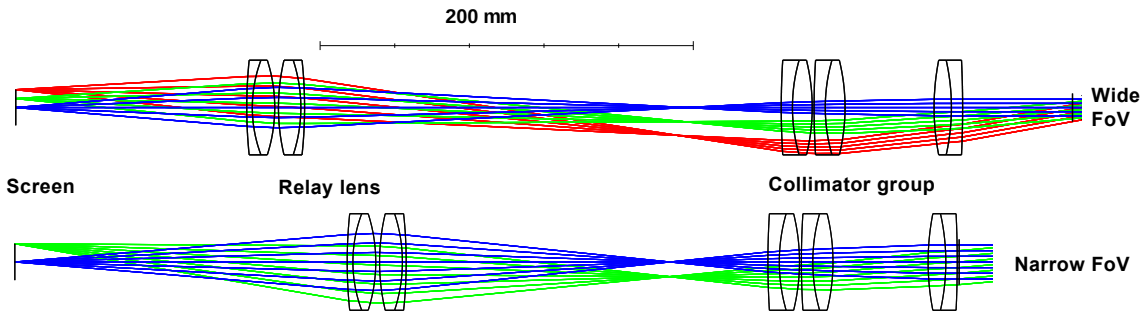

Figure 3. Zemax® optical layout of RETINA for narrow and wide FoV configurations. Three light ray fields are shown for full FoV angles of 0 degrees (blue), 5 degrees (green), and 20 degrees (red).

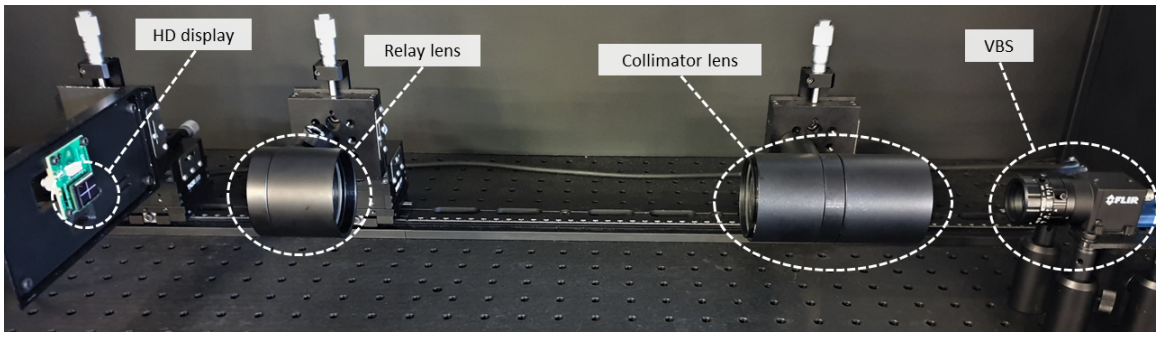

Figure 4. Main components of RETINA.

ity. The software can compute optical aberrations through sequential ray tracing and allows the optimization of several design variables, such as glass materials, curvatures, and thicknesses.

The design of RETINA relies only upon Commerical-Off-The-Shelf (COTS) lens components to lower costs by avoiding the expensive design and manufacturing of custom lenses. This approach makes the optical design a challenging task as it is not possible to fine-tune the characteristics of each component. In particular, the only design variables that can be optimized are the COTS lenses and the distances between them. Because of this, it can be more difficult to reach the performance levels of custom-designed optics, and multiple iterations may be required.[17,18]

To simplify the design process, only achromatic doublet lenses are used. These are constituted by a double layer of glass optimized to reduce aberrations, especially chromatic ones. Thanks to the software it has been possible to test the performance of each candidate solution in different working conditions to ensure consistency throughout the required FoV range. The final design, shown in Figure 3, requires a total of five lenses. Three of them are part of the collimator optical group, which has a focal length of 86.8 mm. The remaining two form the relay lens group, with a focal length of 82.8 mm. The facility and all of its actual components are shown in Figure 4.

The consistency of the optical performance of this design can verified by looking at Figure 5, which shows the spot diagrams obtained from the simulation of the deployed camera model coupled with 25 mm and 50 mm objectives at f/2.8 aperture. The diagrams are plotted in each configuration

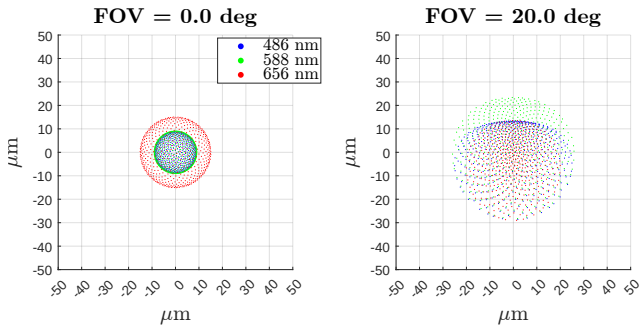

(a) 25 mm objective

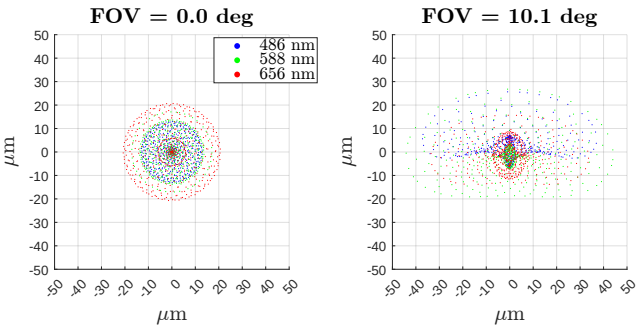

(b) 50 mm objective

Figure 5. Multi-wavelength spot diagrams for axial and maximum FoV light fields for 1/1.8" sensor with 25 mm (a) and 50 mm (b) objective at f/2.8 aperture.

for the maximum FoV and axial light ray fields for three different wavelengths. The RMS radius of the spots varies between 8 and 15 μm in the four presented test cases.

CALIBRATION

Radiometric calibration

The radiometric calibration ensures the correct emulation of the intensity of each object in the synthetic scenes. In other terms, the radiometric calibration is no other than a mapping between the commanded screen pixel digital count and the radiometric intensity experienced by the VBS at its entrance pupil. By reversing the mapping, it is possible to determine the digital count needed to reproduce an object with a given magnitude.

The radiometric characterization of the facility is done using a high-accuracy light power sensor*. The sensor is placed in front of the camera objective to measure the intensity of the collimated light reaching the aperture. Measurements are taken by illuminating squares of N-by-N pixels in the middle of the screen with varying levels of digital count B. Note that, since the sensor is designed to work with monochromatic light, the intensity of the red, green, and blue sub-pixels are to be measured individually. The effective wavelengths of the color channels are determined by converting the CIE curve color points stated by the display datasheet.[19] These are: $\lambda_r = 605$ nm for red, $\lambda_g = 544$ nm for green, and $\lambda_b = 475$ nm for blue.

*Thorlabs S130C product web-page: `https://www.thorlabs.com/thorproduct.cfm?partnumber=S130C`, last visited on Jan 2024.

Figure 6 shows the resulting irradiance measurements I_r, I_g, and I_b respectively for the red, green, and blue channels normalized by the number of pixels for each digital count level B. As the nonlinear trend suggests, a gamma correction curve has been applied to the screen response to increase its range of radiometric representativeness.

Operatively, the conversion between visual magnitude and digital count is carried out as follows. First, the emitting body's spectral irradiance I_λ is computed for a given magnitude m. This is done using the relation:

$$I_\lambda = I_\lambda^0 \cdot 10^{\frac{-m}{2.5}} \tag{7}$$

Where $I_\lambda^0 = 3.67 \cdot 10^{-11}\ \mathrm{W \cdot m^{-2} \cdot nm^{-1}}$ is the spectral irradiance of a zero-magnitude star in the V-band.[20] The conversion between spectral irradiance and screen digital count is not immediate since the screen does not have the same spectral emission as an emitting body. In particular, the emission of an OLED screen is characterized by three peaks in correspondence with each sub-pixel wavelength. Because of this, it is not possible to achieve the full spectral radiometric representativeness of an emitting body. The solution is to ensure that the camera sensor receives the same total effective irradiance that it would experience with a real spectrum. This is the equivalent of verifying that:

$$\int_{\lambda_1}^{\lambda_2} I_\lambda(\lambda) \cdot \eta_\lambda(\lambda)\, d\lambda = \int_{\lambda_1}^{\lambda_2} I_\lambda^s(\lambda, B) \cdot \eta_\lambda(\lambda)\, d\lambda \tag{8}$$

where $I_\lambda^s(\lambda, B)$ is the spectral irradiance of the screen and $\eta_\lambda(\lambda)$ is the relative energetic efficiency of the imaging sensor, expressed as a function of the wavelength λ and defined between λ_1 and λ_2 as:

$$\eta_\lambda(\lambda) = \frac{Q_e(\lambda) \cdot \lambda}{\max\left[Q_e(\lambda) \cdot \lambda\right]} \tag{9}$$

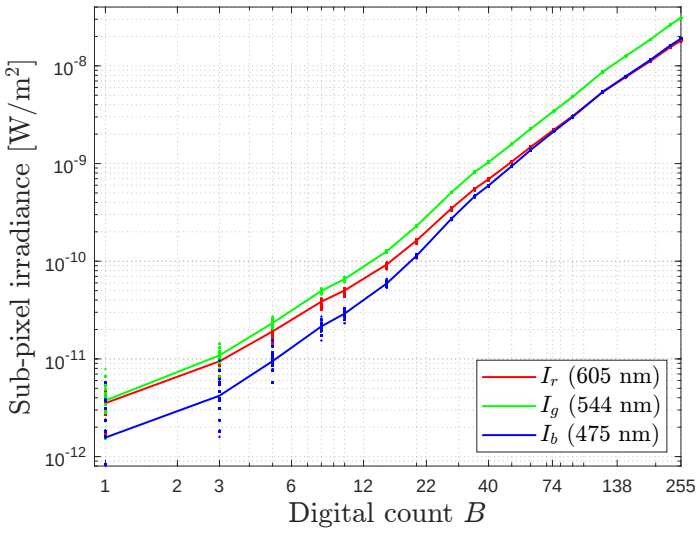

Figure 6. Measured sub-pixel irradiance vs. digital count.

$Q_e(\lambda)$ is the quantum efficiency curve of the sensor, which can be obtained from the camera datasheet.

Two simplifying assumptions are made to ease the calculations. First, the spectral irradiance of the emitting body is considered constant. Second, the irradiance emitted by the screen is considered concentrated in the three emission bands. With those assumptions in place, equation (8) becomes:

$$I_\lambda \int_{\lambda_1}^{\lambda_2} \eta_\lambda(\lambda)\, d\lambda = \eta_\lambda(\lambda_r) I_r(B) + \eta_\lambda(\lambda_g) I_g(B) + \eta_\lambda(\lambda_b) I_b(B) = I_{\text{eff}}(B) \tag{10}$$

For the testing camera, the effective sensor bandwidth $\int_{\lambda_1}^{\lambda_2} \eta_\lambda(\lambda)\, d\lambda$ is determined to be 417 nm, while the values of the three efficiency weighs are: $\eta_\lambda(\lambda_r) = 0.994$, $\eta_\lambda(\lambda_g) = 0.979$, and $\eta_\lambda(\lambda_b) = 0.813$. From equation (10) it is possible to determine the digital count B that is required for emulating a given spectral irradiance I_λ. The drawback of this procedure is that it requires apriori knowledge of the camera response curve to be carried out.

As shown by Beirle et al,[7] the magnification level of the facility influences the calibration, which needs to be updated each time the facility configuration is changed. Figure 7 shows the obtained calibration curve for the wide-FoV testing camera configuration. The curve compares the effective irradiance I_{eff} and the correlated visual magnitude at each digital count level. As reported in the Figure, with this configuration the facility can reproduce emitting sources with magnitudes between -1.44 and 8.25.

To validate the proposed procedure, night sky images of celestial objects are acquired with the test camera. Figure 8 shows the comparison between RETINA photos and the real night-sky counterparts. The two images are acquired with the same camera using the same settings (exposure time, gain, and aperture). Three objects with different magnitude levels are shown. Note that the magnitude of Jupiter at the time of the image was -2.26, which is lower than the minimum magnitude that can be emulated in the facility. Because of this, multiple pixels are lit to produce the same irradiance of the night-sky object. Looking at the images it is possible to notice how the objects in RETINA appear slightly larger and more luminous. This effect is expected for multiple reasons. First, the

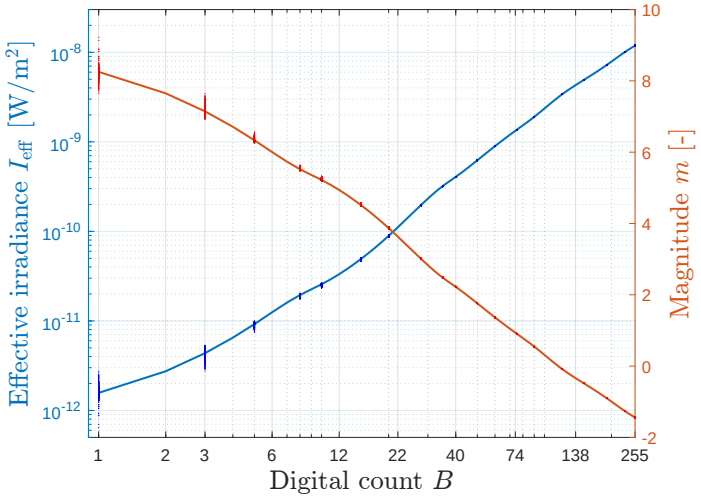

Figure 7. Effective irradiance and emulated magnitude vs. digital count.

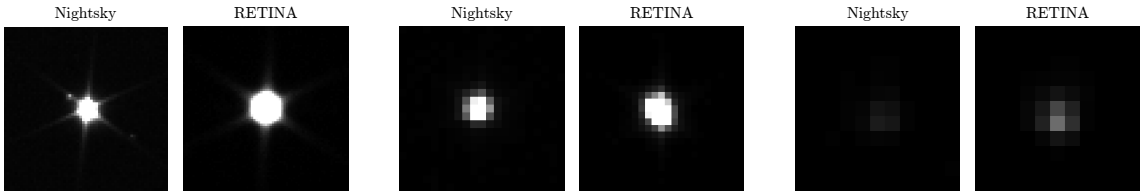

(a) Jupiter m = -2.26 (b) Alnilam (ε-Orionis) m = 1.69 (c) HD 36134 m = 5.94

Figure 8. Comparison between real night-sky images and RETINA images for objects with different magnitudes.

night sky images are affected by atmospheric attenuation and light pollution. In particular, the real images have been acquired in a class-4 Bortle scale region[21] at low elevation angles with strong lunar lighting. These conditions considerably lower the detectability of celestial objects. Second, the pixels of the screen have an angular size which is much larger than the actual stars when observed by the VBS. Third, the additional optical aberrations deriving from the facility spread the light over a wider area.

Projection model

In order to simulate and test IP and VBN algorithms, the facility must reproduce scenes that are geometrically equivalent to those that would be acquired in space by the real VBS. To obtain that, it is necessary to define a projective model that relates the Line-of-Sight (LoS) direction sensed by the VBS with a corresponding location on the screen. In the model, the optical distortions induced by the facility shall be characterized and compensated.[5]

It is assumed that the projective characteristics of the VBS are known. This means that it is always possible to relate a homogenous LoS direction $\boldsymbol{r} = \{r_x, r_y, 1\}^\top$ with the corresponding camera location in the image plane $\boldsymbol{R}^c = \{R_x^c, R_y^c, 1\}^\top$. The generic projection relation is expressed as $\boldsymbol{R}^c = \mathfrak{C}(\boldsymbol{r})$ while the inverse relation is indicated as $\boldsymbol{r} = \mathfrak{C}^{-1}(\boldsymbol{R}^c)$.

The projective relation between screen pixel coordinates $\boldsymbol{R}^s = \{R_x^s, R_y^s, 1\}^\top$ and the undistorted LoSes $\boldsymbol{r}^u = \{r_x^u, r_y^u, 1\}^\top$ is modeled with the pinhole camera model.[22] In particular, the two quantities are linearly related as:

$$\boldsymbol{R}^s = K_f \boldsymbol{r}^u \tag{11}$$

where K_f is a 3-by-3 facility projection matrix:

$$K_f = \begin{bmatrix} f_x & 0 & c_x \\ 0 & f_y & c_y \\ 0 & 0 & 1 \end{bmatrix} \tag{12}$$

The parameters of the K_f matrix are set as follows. The optical center location (c_x, c_y) is set to half of the screen size, assuming perfect alignment between the camera boresight axis and the center of the screen. The two focal lengths f_x and f_y are set to the theoretical value for which the FoV of the facility matrix matches the vertical FoV of the VBS α_v. If n_v is the number of pixels of the screen observed by the camera in the vertical direction, this value can be computed as:

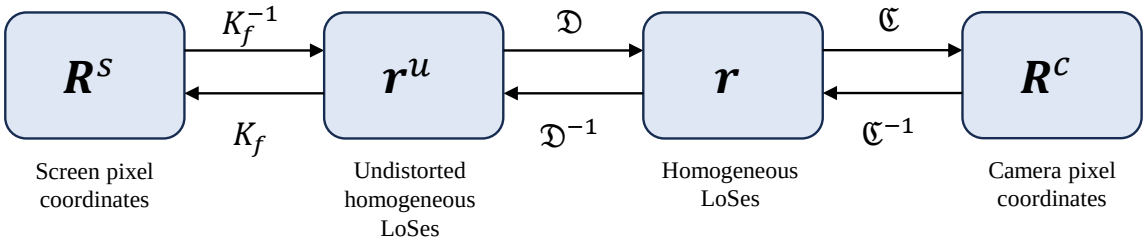

Figure 9. Relations between geometric variables.

$$f_x = f_y = \frac{n_v}{2\tan(\frac{\alpha_v}{2})} \tag{13}$$

It is important to note that the employed pinhole projection model does not account for optical distortions and misalignment between the components of the facility. In order to correct those effects, a polynomial mapping is introduced. The mapping relates the undistorted screen LoSes $\boldsymbol{r}^u$ with the distorted ones $\boldsymbol{r}$ and vice-versa. The direct and inverse transformations are denoted, respectively as $\boldsymbol{r} = \mathfrak{D}(\boldsymbol{r}^u, \boldsymbol{\beta})$ and $\boldsymbol{r}^u = \mathfrak{D}^{-1}(\boldsymbol{r}, \boldsymbol{\gamma})$. $\boldsymbol{\beta}$ and $\boldsymbol{\gamma}$ identify the set of coefficients that characterize the polynomial mapping.

The transformations between the geometric variables are schematized in Figure 9. As it can be seen, to simulate an object at a given LoS $\boldsymbol{r}$ it is first necessary to compensate the optical distortions of the facility using the inverse distortion model $\mathfrak{D}^{-1}$. Then, the screen coordinates are determined by projecting the undistorted LoS via the facility projection matrix K_f.

In general, unresolved objects are reproduced by lighting single pixels on the screen, each with the digital count computed through the radiometric calibration.[1] The pixel that is lit is the one whose center is closer to the required screen coordinates. However, using a single pixel implies a round-off error which is committed each time the intended coordinates do not coincide with the center of a pixel. This means that the error can potentially reach half of the diagonal angular size of a single screen pixel. To eliminate this roundoff error, in RETINA the total irradiance of the object is split among three adjacent pixels. The irradiance distribution is computed to ensure the match between the weighted barycenter of the three pixels and the intended screen coordinates. The effectiveness of this method increases with the irradiance of the represented object since more digital count levels are available to steer the position of the barycenter. This technique allows obtaining sub-pixel accuracy when reproducing unresolved objects at the cost of a slightly increased spot size. Moreover, since multiple pixels are used, it is possible to increment the maximum irradiance that can be emulated in the facility.

The procedure is completely different when simulating resolved objects such as celestial objects and asteroids at close range. In this case, two different strategies can be adopted.[5] In both, the images of the object are rendered assuming as camera characteristics those of the facility projection matrix K_f. The first strategy, named *downstream calibration*, consists of displaying the images in the facility exactly as generated and applying the distortion correction to those acquired by the camera. In the alternative strategy (*upstream compensation*), the screen images are corrected in advance. The advantage of the upstream compensation is that the acquired images can be directly fed

to the IP algorithms without lengthy post-acquisition operations since they are already geometrically equivalent to the real scenarios.

Geometric calibration

The geometric calibration procedure takes care of estimating the coefficients $\boldsymbol{\gamma}$ of the polynomials of the inverse facility distortion model. The procedure is structured as follows. First, a set of calibration images is displayed on the screen and is acquired by the VBS. In each image, hundreds of single pixels distributed throughout the screen are lit. The coordinates of the i-th point $\boldsymbol{R}_i^s$ are converted into undistorted LoSes $\boldsymbol{r}_i^u$ as:

$$\boldsymbol{r}_i^u = K_f^{-1} \boldsymbol{R}_i^s \tag{14}$$

At the same time, the corresponding centroids in the camera images are detected and recognized. The coordinates of the centroids $\hat{\boldsymbol{R}}_i^c$ are converted into distorted LoSes $\hat{\boldsymbol{r}}_i$ through the inverse camera projection model $\mathfrak{C}^{-1}$. Then, the optimal coefficients of the polynomial mapping $\bar{\boldsymbol{\gamma}}$ are found minimizing the total reprojection quadratic residual:

$$\bar{\boldsymbol{\gamma}} = \min_{\boldsymbol{\gamma}} \left(\sum_{i=1}^{N_p} \| \mathfrak{D}^{-1}(\hat{\boldsymbol{r}}_i, \boldsymbol{\gamma}) - \boldsymbol{r}_i^u \|^2 \right) \tag{15}$$

where N_p is the total number of single pixels of the calibration pattern set. The solution is obtained through linear least squares.

The polynomial model used differs from the one of Panicucci et al.[5] In particular, a dependency upon the irradiance of the reproduced pointwise object is introduced to obtain stable calibration accuracy throughout the entire range of radiometric representativeness. Results can be seen in Figure 10, which compares the angular error between the intended LoS direction and the one detected by the VBS for several thousands of pointwise samples with different magnitudes. The tests are

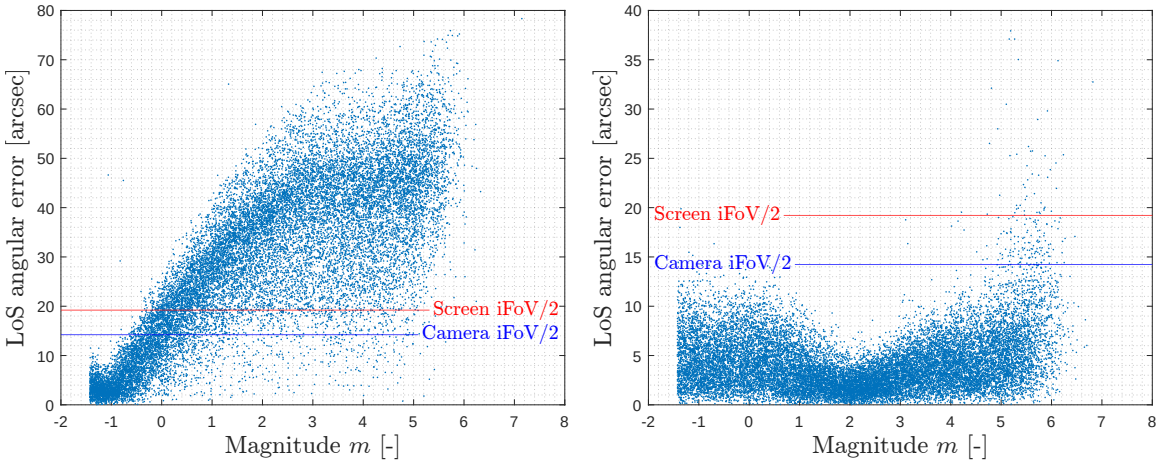

(a) Without irradiance dependency

(b) With irradiance dependency

Figure 10. LoS angular errors with (a) and without (b) irradiance-dependent geometric model using wide-FoV camera configuration.

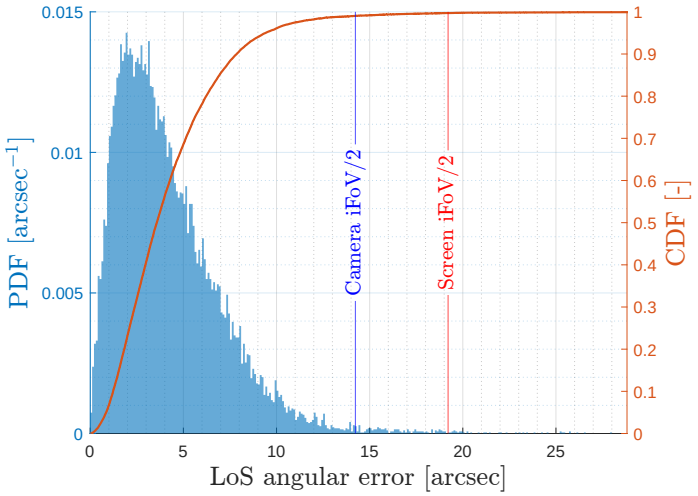

Figure 11. PDF and CDF of LoS angular errors using wide-FoV camera configuration.

conducted with the wide-FoV camera configuration, using the 25 mm objective. As it can be noted, with the simple polynomial model the optimal accuracy is achieved only at irradiance levels similar to those at which the facility has been geometrically calibrated. For different magnitudes, the error grows considerably. This can be attributed to diffraction and asymmetric optical aberrations such as coma which can cause the centroids to shift at different irradiance levels for high FoV angles. Differently, the irradiance-dependent distortion model can compensate for those errors, achieving consistent performance at various magnitudes. The accuracy decreases only at lower illumination levels due to the higher noise influence and the fewer digital count levels available for the sub-pixel correction.

The Probability Density Function (PDF) and Cumulative Distribution Function (CDF) of the overall LoS angular accuracy are shown in Figure 11. The plot demonstrates the capability of emulating radiometrically consistent unresolved objects within 10 arcsec of error in over 96 % of the cases. It must be noted that these results are obtained with the wide-FoV camera configuration, which has a lower angular resolution. The narrow-FoV configuration yields even lower projection errors of 3 arcsec in 99 % of the cases.

APPLICATIONS

Far-range celestial navigation experiment

The first pillar of the EXTREMA project focuses on the development of deep-space autonomous navigation techniques for CubeSats.[9] In particular, the pillar aims at developing and validating a navigation algorithm suitable for deep-space orbit determination during an interplanetary transfer cruise. In that scenario, a probe can determine its state by using planets and other celestial objects as navigation beacons. This technique can be performed in complete autonomy as it relies only on on-board optical cameras to detect the surrounding planetary beacons.[12,23,24] If multiple beacons are acquired at the same time, the position of the spacecraft can be determined analytically knowing the ephemerides of the observed objects. As this is rarely the case, various implementations of the Extended Kalman Filter (EKF) are used to dynamically estimate the complete state of the spacecraft with non-simultaneous measurements.

The details of the EXTREMA navigation algorithm are discussed in Ref. 12 for what concerns the filter implementation and in Ref. 25 for what concerns the IP pipeline. In the algorithm, the images are first processed to detect the coordinates of each centroid. Then, stars are identified through a classic search-less algorithm[26,27] coupled with RANdom SAmple Consensus (RANSAC) to improve the robustness.[28] Using the stars, the attitude of the spacecraft is computed and the planet is recognized. The LoS direction of the planet is then extracted and fed as a measurement to the EKF for state estimation.

To test and validate the image processing pipeline, a set of 5000 images is acquired in the RETINA facility using the wide-FoV camera configuration. Each image depicts deep-space scenarios generated using the HIPPARCOS catalogue.[29] In each pose the satellite has a random position in the solar system and a random planet is observed. Figure 12 shows the CDF of the attitude determination errors for about-boresight and cross-boresight rotations. As expected, the latter are estimated with lower accuracy. For the tested scenarios the attitude is correctly determined in 98.22 % of the cases. When the attitude determination is successful, the planets are identified in 98.82 % of the cases with a 3-σ apriori knowledge of the position of 10^5 km.

The EKF is tested on a reference trajectory targeting a ballistic capture corridor towards Mars.[30] The dynamics of the high-fidelity reference trajectory include perturbations due to solar radiation pressure, third-body accelerations from all the planets in the Solar System, and relativistic effects. Every 10 days during the trajectory a navigation session is performed. During each session, a total of 72 images are acquired every 100 seconds targeting two different planets. All the navigation images are simulated in the RETINA facility and fed to the IP.

Figure 13 shows the results of a Montecarlo simulation performed using the acquired images. In each of the 100 samples, the filter starts with a randomly selected initial condition. As shown by the position and velocity estimation errors, all the samples converge within the estimated 3-σ bounds. At the end of the trajectory, the position and the velocity are respectively estimated with a 3-σ accuracy of 5320 km and 0.97 m/s.

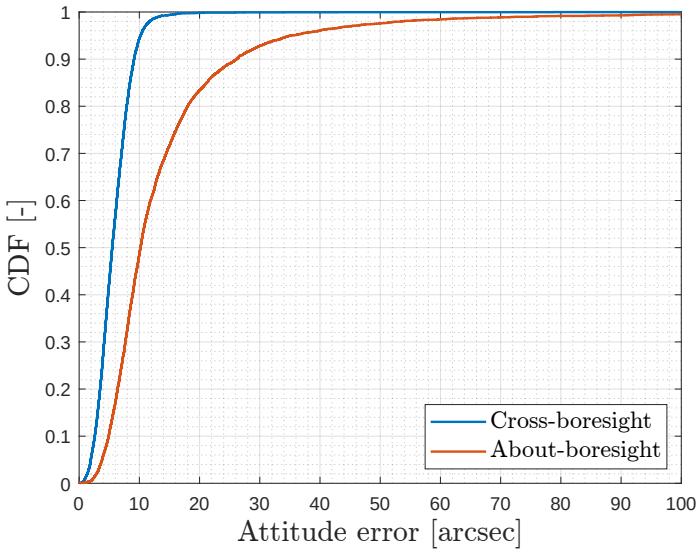

Figure 12. CDF of attitude determination errors.

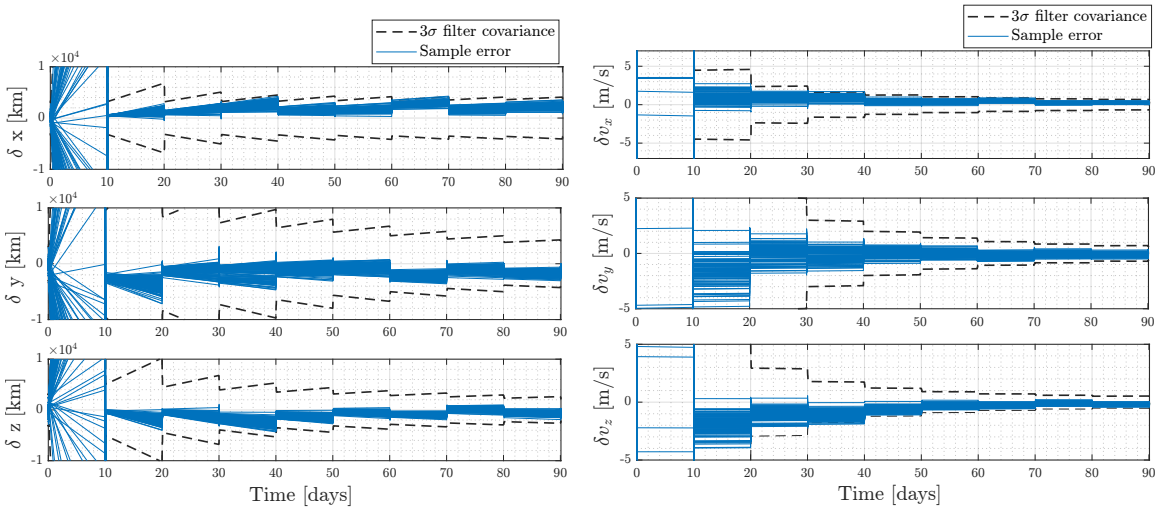

(a) Position error

(b) Velocity error

Figure 13. Filtered position (a) and velocity (b) errors in ecliptic J2000 frame for the tested samples.

LUMIO navigation experiment

LUMIO (Lunar Meteoroid Impacts Observer) is a proposed lunar exploration mission that has the goal of detecting, quantifying, and characterizing the impacts of near-Earth meteoroids on the lunar far side.[14,31] The mission will be carried out by a 12-U CubeSat operating from a quasi-halo orbit around the L2 lagrangian point of the Earth-Moon system. The main payload of the mission is the LUMIO Cam, a high-end imaging camera with a FoV of 6 degrees that will monitor the Moon. In addition to its scientific tasks, the camera will be used for a vision-based navigation experiment to prove the capability of navigating in complete autonomy.[15,32]

The technique used in the experiment is called full disk navigation as it involves full-size images of the lunar face. First, the images are processed to detect the location of the points belonging to the lunar limb with subpixel accuracy. Outliers are rejected using RANSAC by fitting a circumference through the set of points. Then, the limb points are used as measurements in an extended Kalman filter to estimate the state of the spacecraft relative to the Moon.[32]

A simulation is carried out in the RETINA facility to test the performance of the IP pipeline of the LUMIO navigation experiment when subjected to real camera images. The test camera in these simulations is set with a narrow FoV configuration which has the same FoV as the LUMIOCam. A set of 4321 synthetic images is generated using CORTO, the Blender-based celestial rendering tool developed at the DART group.[33] The images are generated every 300 s and cover 15 days of the LUMIO trajectory. The images acquired in the facility, such as the example of Figure 14, are warped to remove optical distortions using the downstream compensation procedure.[5]

Figure 15 shows the performance reached by the LUMIO navigation filter for the three components of the camera reference frame. As expected, the position along the Z-axis is estimated with less accuracy than the X and Y components. The results shown in the Figure are similar to those obtained with only synthetic renderer images.[32]

Figure 14. Example of lunar far side image acquired in RETINA.

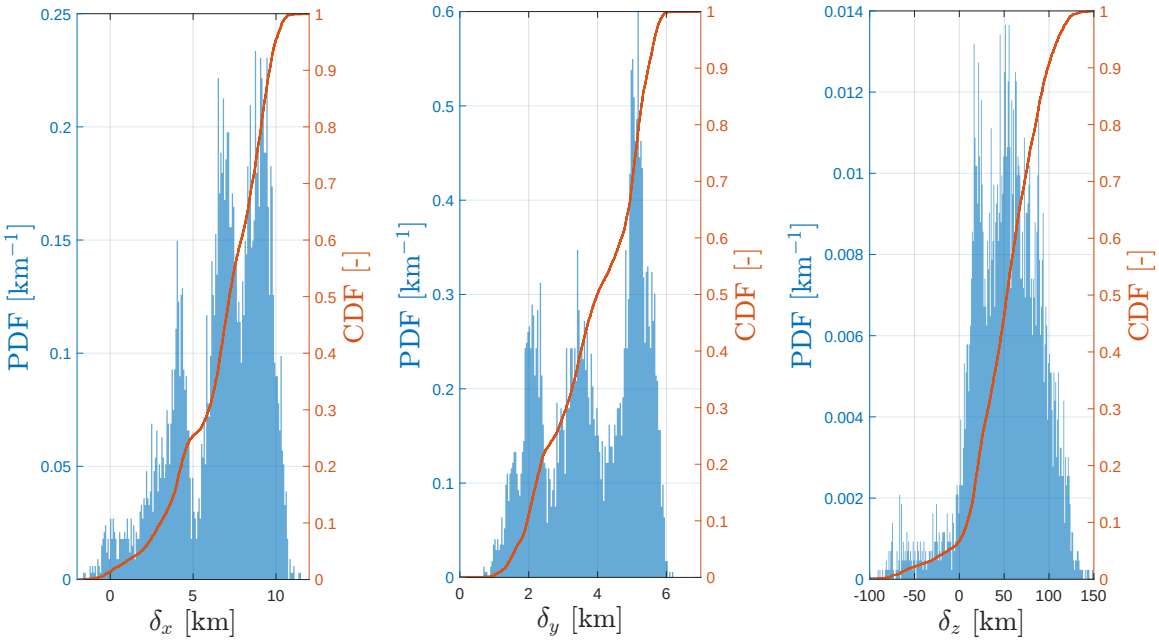

Figure 15. PDF and CDF of the position error in camera frame as estimated by the LUMIO navigation filter during the sampled trajectory.

CONCLUSIONS

This work presents the development of RETINA, a new optical facility for performing hardware-in-the-loop simulations of vision-based sensors. The facility is composed of a high-resolution and a twin-lens variable magnification optical system. The variable-magnification architecture guarantees flexibility in the deployment of cameras with different characteristics. In particular, the facility is designed with the intent of testing CubeSat-compatible cameras with a field of view between 4 and 22 degrees. The optical magnification of RETINA can be modified by adjusting the relative position of its components to ensure the maximum resolution of the reproduced scenes in any FoV condition.

The optical behavior of the facility has been analyzed using a simplified paraxial model to assess the constraints deriving from the design requirements. This has allowed the definition of clear boundaries for characteristics of the selectable hardware components. Thanks to an optical design software, it has been possible to identify the commercial off-the-shelf components needed for achieving a suitable imaging quality. The design is optimized to guarantee consistent optical performance throughout the working FoV range.

The procedures for the radiometric and geometric calibration are also shown. The first is performed through a high-accuracy light power meter to asses the radiometric response of the facility. This has allowed the characterization of a mapping between the screen digital count of the screen and the corresponding emulated visual magnitude. In particular, with the tested setup it is possible to reproduce the brightness level of objects between -1.44 and 8.25. Thanks to the geometric calibration procedure it has been possible to characterize the optical distortions induced by the optical system of the facility. A new irradiance-dependent geometric model has been used to ensure consistent accuracy at different brightness values. The model allows the compensation of the optical distortions for reproducing scenes that are geometrically equivalent to those that would be observed in a real scenario. An overall accuracy 10 arcsec in over 96 % of the cases is verified in a wide-FoV camera configuration.

The developed test bench is a valuable tool for assessing the functionality, reliability, and accuracy of vision-based navigation algorithms. Two experimental examples are provided. In the first, the autonomous celestial navigation and image processing pipelines developed within the EXTREMA project are tested with real images acquired in the facility. Two datasets are acquired, one involving the random poses to determine the accuracy of the attitude determination and one simulating a deep-space transfer trajectory to validate the performance of the navigation filter. In the second experimental example, a set of images of the lunar far side is acquired to validate the full-disk optical navigation algorithm of the LUMIO CubeSat mission.

AKNOWLEDGEMENTS

This research is part of EXTREMA, a project that has received funding from the European Research Council (ERC) under the European Union's Horizon 2020 research and innovation programme (Grant Agreement No. 864697).

REFERENCES

[1] G. Rufino and A. Moccia, "Laboratory test system for performance evaluation of advanced star sensors," *Journal of Guidance, Control, and Dynamics*, Vol. 25, No. 2, 2002, pp. 200–208. DOI: 10.2514/2.4888.

[2] G. Rufino, D. Accardo, M. Grassi, G. Fasano, A. Renga, and U. Tancredi, "Real-time hardware-in-the-loop tests of star tracker algorithms," *International Journal of Aerospace Engineering*, 2013. DOI: 10.1155/2013/505720.

[3] M. A. Samaan, S. R. Steffes, and S. Theil, "Star tracker real-time hardware in the loop testing using optical star simulator," *Spaceflight Mechanics*, Vol. 140, 2011.

[4] N. Filipe, L. Jones-Wilson, S. Mohan, K. Lo, and W. Jones-Wilson, "Miniaturized star tracker stimulator for closed-loop testing of cubesats," *Journal of Guidance, Control, and Dynamics*, Vol. 40, No. 12, 2017, pp. 3239–3246. DOI: 10.2514/1.G002794.

[5] P. Panicucci and F. Topputo, "The TinyV3RSE Hardware-in-the-Loop Vision-Based Navigation Facility," *Sensors*, Vol. 22, No. 23, 2022, p. 9333. DOI: 10.3390/s22239333.

[6] M. Pugliatti, V. Franzese, P. Panicucci, and F. Topputo, "TINYV3RSE: The DART Vision-Based Navigation Test-bench," *AIAA Scitech 2022 Forum*, 2022, p. 1193.

[7] C. Beierle and S. D'Amico, "Variable-Magnification Optical Stimulator for Training and Validation of Spaceborne Vision-Based Navigation," *Journal of Spacecraft and Rockets*, Vol. 56, No. 4, 2019, pp. 1060–1072. DOI: 10.2514/1.A34337.

[8] D. Roessler, D. A. Pedersen, M. Benn, and J. L. Jørgensen, "Optical stimulator for vision-based sensors," *Advanced Optical Technologies*, Vol. 3, No. 2, 2014, pp. 199–207, doi:10.1515/aot-2013-0045.

[9] G. Di Domenico, E. Andreis, A. Carlo Morelli, G. Merisio, V. Franzese, C. Giordano, A. Morselli, P. Panicucci, F. Ferrari, and F. Topputo, "The ERC-Funded EXTREMA Project: Achieving Self-Driving Interplanetary CubeSats," *Modeling and Optimization in Space Engineering: New Concepts and Approaches*, pp. 167–199, Springer, 2022. DOI: 10.1007/978-3-031-24812-2_6.

[10] G. Di Domenico, E. Andreis, A. C. Morelli, G. Merisio, V. Franzese, C. Giordano, A. Morselli, P. Panicucci, F. Ferrari, and F. Topputo, "Toward Self-Driving Interplanetary CubeSats: the ERC-Funded Project EXTREMA," *72nd International Astronautical Congress (IAC 2021)*, 2021, pp. 1–11.

[11] P. Panicucci, E. Andreis, V. Franzese, F. Topputo, *et al.*, "An Overview of the EXTREMA Deep-Space Optical Navigation Experiment," *3rd Space Imaging Workshop*, 2022, pp. 1–3.

[12] E. Andreis, V. Franzese, and F. Topputo, "Onboard Orbit Determination for Deep-Space CubeSats," *Journal of Guidance, Control, and Dynamics*, Vol. 45, No. 8, 2022, pp. 1466–1480. DOI: 10.2514/1.G0062941.

[13] A. Morselli, G. Di Domenico, E. Andreis, A. C. Morelli, G. Merisio, V. Franzese, C. Giordano, P. Panicucci, F. Ferrari, and F. Topputo, "The EXTREMA Orbital Simulation Hub: a Facility for GNC Testing of Autonomous Interplanetary CubeSat," *4S Symposium*, 2022, pp. 1–13.

[14] S. Speretta, A. Cervone, P. Sundaramoorthy, R. Noomen, S. Mestry, A. Cipriano, F. Topputo, J. Biggs, P. Di Lizia, M. Massari, *et al.*, "LUMIO: an autonomous CubeSat for lunar exploration," *Space operations: inspiring Humankind's future*, 2019, pp. 103–134. DOI: 10.1007/978-3-030-11536-4_6.

[15] V. Franzese, P. Di Lizia, and F. Topputo, "Autonomous optical navigation for lumio mission," *2018 Space Flight Mechanics Meeting*, 2018, p. 1977. DOI: 10.2514/6.2018-1977.

[16] P. Panicucci, F. Piccolo, A. Rizza, F. Topputo, and R. Walker, "Vision-Based Navigation for the LUMIO CubeSat Mission," *46th Annual AAS Guidance, Navigation and Control Conference*, 2024.

[17] L. Ryzhikov, R. B. Johnson, V. N. Mahajan, S. Thibault, and A. Padilla-Vivanco, "Method for designing optical systems from the off-the-shelf optical components," *Current Developments in Lens Design and Optical Engineering XXIII*, Vol. 12217, International Society for Optics and Photonics, SPIE, 2022, p. 122170W. DOI: 10.1117/12.2627980.

[18] A. Madrid-Sánchez, J. Ortiz-Ocampo, C. Trujillo, and H. Ottevaere, "Off-the-shelf optical systems design enabled by an evolution strategy: front stop case," *Journal of Physics: Photonics*, Vol. 6, No. 1, 2023, p. 015002, 10.1088/2515-7647/ad10b2.

[19] J. Schanda, *Colorimetry: understanding the CIE system*. John Wiley & Sons, 2007.

[20] L. Colina, R. Bohlin, and F. Castelli, "Absolute flux calibrated spectrum of Vega," *Instrument Science Report CAL/SCS-008, Space Telescope Science Institute*, 1996.

[21] J. E. Bortle, "The Bortle Dark-Sky Scale," *Sky and Telescope*, 2001.

[22] R. Hartley and A. Zisserman, *Multiple view geometry in computer vision*. Cambridge university press, 2003.

[23] R. Raymond Karimi and D. Mortari, "Interplanetary autonomous navigation using visible planets," *Journal of Guidance, Control, and Dynamics*, Vol. 38, No. 6, 2015, pp. 1151–1156.

[24] S. Henry and J. A. Christian, "Absolute triangulation algorithms for space exploration," *Journal of Guidance, Control, and Dynamics*, Vol. 46, No. 1, 2023, pp. 21–46.

[25] E. Andreis, P. Panicucci, V. Franzese, F. Topputo, *et al.*, "A Robust Image Processing Pipeline for Planets Line-Of-Sight Extraction for Deep-Space Autonomous Cubesats Navigation," *44th AAS Guidance, Navigation and Control Conference*, 2023, pp. 1–19.

[26] D. Mortari, "Search-less algorithm for star pattern recognition," *The Journal of the Astronautical Sciences*, Vol. 45, 1997, pp. 179–194.

[27] D. Mortari, M. A. Samaan, C. Bruccoleri, and J. L. Junkins, "The pyramid star identification technique," *Navigation*, Vol. 51, No. 3, 2004, pp. 171–183.

[28] M. A. Fishler, "Random sample consensus: A paradigm for model fitting with applications to image analysis and automated cartography," *Commun, ACM*, Vol. 24, No. 6, 1981, pp. 381–395.

[29] M. A. Perryman, L. Lindegren, J. Kovalevsky, E. Hoeg, U. Bastian, P. Bernacca, M. Crézé, F. Donati, M. Grenon, M. Grewing, *et al.*, "The HIPPARCOS catalogue," *Astronomy and Astrophysics, Vol. 323, p. L49-L52*, Vol. 323, 1997, pp. L49–L52.

[30] G. Merisio, F. Topputo, *et al.*, "Characterization of ballistic capture corridors aiming at autonomous ballistic capture at Mars," *2021 AAS/AIAA Astrodynamics Specialist Conference*, 2022, pp. 1–21.

[31] F. Topputo, G. Merisio, V. Franzese, C. Giordano, M. Massari, G. Pilato, D. Labate, A. Cervone, S. Speretta, A. Menicucci, *et al.*, "Meteoroids detection with the LUMIO lunar CubeSat," *Icarus*, Vol. 389, 2023, p. 115213.

[32] P. Panicucci, F. Piccolo, S. Borgia, A. Rizza, V. Franzese, F. Topputo, *et al.*, "Current status of the lumio autonomous optical navigation experiment," *12th International Conference on Guidance, Navigation & Control Systems (GNC) and 9th International Conference on Astrodynamics Tools and Techniques (ICATT)*, 2023, pp. 1–15.

[33] M. Pugliatti, C. Buonagura, and F. Topputo, "CORTO: The Celestial Object Rendering TOol at DART Lab," *Sensors*, Vol. 23, No. 23, 2023, p. 9595.